

A regime diagram for the slurry F-layer at the base of Earth's outer core

Jenny Wong^{a,b,*}, Christopher J. Davies^c, Christopher A. Jones^d

^a*Université de Paris, Institut de physique du globe de Paris, CNRS, F-75005 Paris, France*

^b*EPSRC Centre for Doctoral Training in Fluid Dynamics, University of Leeds, Leeds, LS2 9JT, UK*

^c*School of Earth and Environment, University of Leeds, Leeds, LS2 9JT, UK*

^d*School of Mathematics, University of Leeds, Leeds, LS2 9JT, UK*

Abstract

Seismic observations of a slowdown in P wave velocity at the base of Earth's outer core suggest the presence of a stably-stratified region known as the F-layer. This raises an important question: how can light elements that drive the geodynamo pass through the stably-stratified layer without disturbing it? We consider the F-layer as a slurry containing solid particles dispersed within the liquid iron alloy that sink under gravity towards the inner core. We present a regime diagram showing how the dynamics of the slurry F-layer change upon varying the key parameters: Péclet number (Pe), the ratio between advection and chemical diffusion; Stefan number (St), the ratio between sensible and latent heat; and Lewis number (Le), the ratio between thermal and chemical diffusivity. We obtain four regimes corresponding to stable, partially stable, unstable and no slurries. No slurry is found when the heat flow at the base of the layer exceeds the heat flow at the top, while a stably-stratified slurry arises when advection overcomes thermal diffusion ($Pe \gtrsim Le$) that exists over a wide range of parameters relevant to the Earth's core. Our results estimate that a stably-stratified F-layer gives a maximum inner-core boundary (ICB) body

*Corresponding author

Email address: wong@ipgp.fr (Jenny Wong)

wave density jump of $\Delta\rho_{\text{bod}} \leq 534 \text{ kgm}^{-3}$ which is compatible with the lower end of the seismic observations where $280 \leq \Delta\rho_{\text{bod}} \leq 1,100 \text{ kgm}^{-3}$ is reported in the literature. With high thermal conductivity the model predicts an inner core age between 0.6 and 1.2 Ga, which is consistent with other core evolution models. Our results suggest that a slurry model with high core conductivity predicts geophysical properties of the F-layer and core that are consistent with independent seismic and geodynamic calculations.

Keywords: slurry, iron snow, inner core, crystallisation, F-layer

1. Introduction

Seismic, geomagnetic and dynamical explanations for and against the presence of stably-stratified layers in the Earth's liquid core is an active research topic of significant geophysical interest. Confirmation of their existence would warrant a shift away from the usual approximation that the core is adiabatically stratified with thin boundary layers. Stably-stratified layers should exhibit dynamics that distinguish them from the turbulent bulk of the core; elucidating this behaviour will help to uncover their signature in seismic and geomagnetic observations [1]. In this paper we focus on the F-layer at the base of the liquid core to further understand the conditions where stable stratification can be sustained.

There is a strong consensus that a slowdown in the P wave velocity compared with the Preliminary Reference Earth Model (PREM) [2] is observed at the base of the Earth's outer core [3, 4, 5]. PREM follows the Adams-Williamson equation that assumes the outer core is adiabatically stratified and homogeneous throughout, therefore a P wave velocity lower than PREM is attributed to an anomalously higher density structure than expected. This departure in density away from neutral stability means that the seismic observations suggest a stably-stratified layer exists that cannot be explained by adiabatic compression alone.

Estimates of the layer thickness vary from 150 km [3] to 400 km [4] thick, which greatly exceeds the thermal diffusion length scale, hence the layer cannot be simply explained by a thermal boundary layer alone and another mechanism is required to maintain stratification [6].

The F-layer is intimately linked to the geodynamo process that generates Earth's magnetic field. Motion of the liquid iron core is powered by heat extracted at the core-mantle boundary (CMB), which leads to freezing of the solid inner core from the centre of the Earth because the melting curve is steeper than the core adiabat. Freezing releases latent heat and light elements into the liquid; light elements drive compositional convection in the core and is thought to be the main power source for the dynamo at the present day [7]. The key issue is buoyant light material excluded from the inner core must pass through the F-layer and into the overlying core while preserving stable stratification.

Previous geodynamic models try to explain the F-layer by inner core translation [8], a thermochemical layer [9], or a slurry (iron snow) layer [10, 11]. Inner core translation supposes melting occurs on the eastern hemisphere of the inner core while freezing occurs on the western hemisphere to form a dense layer above the inner-core boundary (ICB), though recent upward revisions of the thermal conductivity of iron [12, 13] together with the likely presence of compositionally stabilising conditions suggest that the instability cannot arise in the present-day [14, 15]. [9] proposed a thermochemical model with the F-layer on the liquidus that succeeded in producing a stably-stratified layer, however, the model effectively imposed a stable composition without a physical mechanism explaining why. Wong *et al.* [11] explains this mechanism in a self-consistent way by proposing a slurry layer that captures the physics of how light element and solid is transported. The authors used a simple box model to demonstrate that a slurry layer produced stably-stratified layers that match the seismic ob-

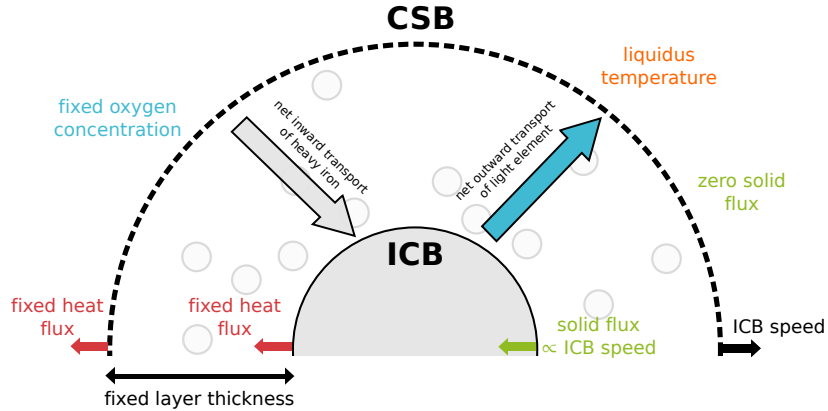


Figure 1: A sketch of the slurry layer at the base of Earth’s outer core, with the boundary conditions imposed at the inner core boundary (ICB) and core slurry boundary (CSB) described in Section 2.

servations of density and layer thickness. In this work we focus on the slurry scenario and build upon Wong *et al.* [11], hereafter referred to as W18.

In the slurry, pure solid iron particles crystallise throughout the entire F-layer while light elements remain in the liquid (see Figure 1 for a sketch). Heavy grains of iron fall under gravity to accumulate at the base of the layer, thereby producing a net inward transport of dense solid and a net outward transport of light elements to give an overall stable density stratification. W18 simplified the full slurry theory by Loper and Roberts [10, 16] and developed a reduced, thermodynamically self-consistent framework that accounts for solid and liquid phase, in addition to the influence of pressure, temperature and composition. The fraction of solid in a slurry is assumed to be small, and so cannot transmit shear waves to create an impedance contrast at the top of the F-layer that would otherwise have been seismically observable.

The principal assumptions of the W18 slurry model are (1) the fast-melting limit and (2) a binary alloy. (1) supposes that an infinitesimal material volume contains either solid or liquid phase exclusively so that the system is in phase

equilibrium. As a consequence, minimising the Gibbs free energy constrains the slurry temperature to the liquidus. (2) presumes an Fe-O composition since oxygen is able to explain the core density deficit [17]. *Ab initio* calculations show that oxygen almost entirely partitions into the liquid phase upon freezing [18] and cannot occur with silicon (another potential light element candidate) in large quantities [19]. The solid produced by the slurry is thereby assumed to be composed of pure iron, which avoids a complicated particle history dependence that would be difficult to model, where the growth of solid grains at different pressure-temperature conditions affects the composition of light elements in the solid.

We generalise the W18 model by moving from a Cartesian to spherical geometry and update the boundary conditions to a more geophysically realistic setup. We suppose that the inner core is isothermal and not convecting due to the upward revisions of the thermal conductivity [20, 21] of iron alloys at core conditions, which means that the present-day inner core is unlikely to convect. We consider a thin compacting layer on the order of kilometres thick on the solid side of the inner core [22], parameterised by interfacial freezing at the ICB which generates a flux of latent heat into the slurry. Accordingly, the ICB advances at a rate composed of the interfacial freezing speed and the snow speed given by the accumulation of solid iron particles from the slurry. Our model self-consistently determines the ICB speed and therefore allows the inner core growth rate to be independently determined, whereas this was fixed in W18 and yielded unrealistically high ICB heat flows. Following the fast-melting limit, we set the temperature at the top of the layer to the liquidus temperature for the bulk core composition obtained from the literature, so that the ICB temperature is free to be self-determined by the slurry whereas this was fixed in W18.

In this paper, we perform a systematic parameter search to elucidate the

conditions that promote stable stratification of the F-layer. The generalised model of W18 and the derivation of the dimensionless system with its associated dimensionless control parameters is given in Section 2. In Section 3, we present and discuss example solutions of the temperature, oxygen concentration, solid flux and density given by the slurry model with different layer thicknesses. We proceed to test the sensitivity of the model to the boundary conditions on the temperature and composition at the top of the layer, before mapping a regime diagram of the slurry based on the main dimensionless control parameters. This vastly improves upon the computed solution space of W18 and uncovers the possible regimes occupied by the slurry. We demonstrate the predictive power of our model for seismic observations and inner core age, before concluding with a summary of our findings in Section 4.

2. Model and Methods

2.1. Dimensional equations

Detailed development of the slurry model is given W18 so here we present the key details. We start with the general equations for the conservation of oxygen, temperature and the liquidus constraint from W18 (equations (4),(6) and (13)), given by

$$\rho^{sl} \frac{D\xi}{Dt} = -\nabla \cdot \mathbf{i}, \quad (1)$$

$$\rho^{sl} c_p \frac{DT}{Dt} = \nabla \cdot (k\nabla T + L\mathbf{j}) + \rho^{sl} L \frac{D\phi}{Dt}, \quad (2)$$

$$\nabla T = \frac{T\Delta V_{Fe}^{s,l}}{L} \nabla p - \frac{T\xi^l (\partial\mu/\partial\xi^l)}{L} \nabla \xi^l, \quad (3)$$

where p is the pressure, T is the temperature, ξ is the oxygen concentration, ξ^l is the oxygen concentration in the liquid phase, ϕ is the solid fraction, ρ^{sl} is the reference density of the slurry taken to be the PREM value at the CSB, \mathbf{i}

is the oxygen flux vector, \mathbf{j} is the solid flux vector, c_p is the specific heat capacity, k is the thermal conductivity, L is the latent heat of fusion, $\Delta V_{Fe}^{s,l}$ is the change in specific volume between liquid iron and solid iron, and $\partial\mu/\partial\xi^l$ is the thermodynamic derivative of the chemical potential, μ , with respect to ξ^l . Throughout this paper superscripts s , l and sl denote solid, liquid or slurry phases respectively, and subscripts Fe and O denote the iron and oxygen components, respectively. For further reference, a table of symbols and values is provided in Appendix A, Table A.2.

We adopt a spherical, one-dimensional geometry where we assume a global F-layer in a non-convective steady state that depends on radius only and excludes lateral variations. The layer thickness, d , is fixed so that the slurry is defined over the interval $[r^i, r^{sl}]$, where r^i denotes the ICB radius and $r^{sl} \equiv r^i + d$ is the core-slurry boundary (CSB). We are interested in a timescale that is long compared with the timescale of freezing and comparable to the evolution of the inner core [23], so we assume a Boussinesq slurry with a reference state in hydrostatic equilibrium, and resolve the slurry layer in a frame moving at the rate of inner core growth, $v\hat{\mathbf{f}}$, with v the ICB speed and $\hat{\mathbf{f}}$ the unit vector pointing outwards and normal to the inner core surface. Mass conservation $\nabla \cdot \mathbf{v} = 0$ implies that $v(r) = v^i(r^i/r)^2$, where the changes in ICB speed due to radius are negligible and we therefore assume that v is constant. This speed is composed of two parts, $v = v_s + v_f$, where v_s is the snow speed, in which all solid particles from the slurry are assumed to accumulate at the base of the layer; and v_f is the freezing speed, which represents the growth of the inner core due to compaction on the solid side of the ICB, and assumed to occur quickly compared with the slurry timescale. The material derivative is hence $D/Dt \rightarrow -v d/dr$. As in W18, the fraction of solid, ϕ , in the slurry is small so that $\phi \ll 1$, and we assume that their variations, $d\phi$, are negligible (see discussion in Appendix B).

We apply the above assumptions to equations (1 – 3), to obtain,

$$-v\rho^{sl}\frac{d\xi^l}{dr} = \frac{1}{r^2}\frac{d}{dr}\left(r^2\frac{\rho^{sl}\Delta V_{Fe,O}^{s,l}D_O}{RT\frac{1000}{a_O}}\exp\left(\frac{F(r-r^i)}{d}\right)\frac{dp}{dr}\right) + \xi^l\frac{dj}{dr} + j\frac{d\xi^l}{dr} + \frac{2}{r}\xi^lj, \quad (4)$$

$$-v\rho^{sl}c_p\frac{dT}{dr} = k\frac{d^2T}{dr^2} + \frac{2}{r}k\frac{dT}{dr} + L\frac{dj}{dr} + \frac{2}{r}Lj, \quad (5)$$

$$\frac{dT}{dr} = -\frac{T\Delta V_{Fe}^{s,l}}{L}g\rho - \frac{RT^21000}{a_O L}\frac{d\xi^l}{dr}. \quad (6)$$

On the LHS of (4), we have the advection of oxygen, and on the RHS, the first term is the effect of barodiffusion and the last three terms describe the physical displacement of oxygen as solid iron particles sediment. On the LHS of (5), we have the advection of heat, and on the RHS, the first two terms correspond to thermal diffusion and the last two terms correspond to the latent heat release associated with phase change. The liquidus constraint (6) describes the change in the liquidus temperature as a consequence of changes in pressure, given by the first term on the RHS, and changes in composition, given by the second term on the RHS.

We have applied ideal solution theory [24] so that the thermodynamic derivative of the chemical potential with respect to ξ^l can be expressed as $\xi^l\partial\mu/\partial\xi^l = RT1000/a_O$, where R is the gas constant and a_O is the atomic weight of oxygen. We expect penetrative convection to occur at the top of the layer because of the velocity difference between the non-convective slurry and the overlying convective outer core. We have thus invoked a turbulent mixing sublayer below the CSB that promotes the transport of oxygen out of the layer and also allows us to impose a vanishing solid flux boundary condition at the CSB (see equation (10) below). This effect is modelled by modifying the self-diffusion coefficient

of oxygen to take the exponential form

$$\bar{D} = D_O \exp\left(\frac{F(r - r^i)}{d}\right), \quad (7)$$

where F is the mixing parameter that appears in the first term on the RHS of (4), and D_O is the self-diffusion coefficient of oxygen taken from the literature [25].

2.2. Boundary conditions

We have three equations (4),(5), and (6) for three output variables T, ξ^l, j , and two output parameters (eigenvalues) F and v . The system is fourth order, therefore we require six boundary conditions to determine a unique solution. We suppose that the oxygen concentration is constant at the CSB and equal to the uniform value in the bulk of the core, ξ^{sl} , since the liquid core is vigorously convecting and its composition does not change much over the timescales considered [26], so that

$$\xi^l(r^{sl}) = \xi^{sl}. \quad (8)$$

At the ICB the solid flux is proportional to the ICB speed and at the CSB the solid flux vanishes, so that

$$j(r^i) = -\rho_-^s v, \quad (9)$$

$$j(r^{sl}) = 0, \quad (10)$$

where ρ_-^s denotes the density on the solid side of the ICB.

We fix the heat flux per unit area at the CSB to a constant value, q^{sl} , and this is a parameter to be varied since there are no independent estimates. By

Fourier's law, the boundary condition on the CSB temperature gradient is

$$\left. \frac{dT}{dr} \right|_{r=r^{sl}} = -\frac{q^{sl}}{k}. \quad (11)$$

In the following two boundary conditions, we digress from the conditions imposed in W18. First, compaction below the F-layer releases latent heat at the interface while there is no specific heat contribution from an isothermal IC, whereas W18 assumed specific heat loss from the inner core. Second, we assume that the temperature at the top of the layer is coincident with the liquidus temperature of the bulk composition, $T^{sl}(r^{sl})$, known from estimates given in the literature [25, 27], so that

$$\left. \frac{dT}{dr} \right|_{r=r^i} = -\frac{\rho^s v_f L}{k} = -\frac{q^s}{k}, \quad (12)$$

$$T(r^{sl}) = T^{sl}(r^{sl}). \quad (13)$$

where q^s is the ICB heat flux per unit area.

2.3. Dimensionless equations

We derive the dimensionless equations using the following scalings,

$$\begin{aligned} r &= r^{sl} \hat{r}, & T &= \frac{q^{sl}}{\rho^{sl} c_p v_f} \hat{T}, \\ \xi^l &= \xi^{sl} \hat{\xi}, & j &= \rho^s v_f \hat{j}, \\ g &= g^{sl} \hat{g}, & \rho &= \rho^{sl} \hat{\rho}, \\ v &= v_f \hat{v} \end{aligned} \quad (14)$$

where the hat symbol denotes a dimensionless quantity that depends on radius. The slurry layer is defined over the dimensionless interval $[r^i/r^{sl}, 1]$. Equations

(4)–(6) respectively become

$$-\hat{v} \frac{d\hat{\xi}}{d\hat{r}} = -\frac{1}{\hat{r}^2} \frac{d}{d\hat{r}} \left(\frac{Li_p R_\rho}{Li_\xi Pe St R_v} \frac{\hat{g} \hat{\rho} \hat{r}^2}{\hat{T}} \exp \left[\frac{F(r^{sl} \hat{r} - r^i)}{d} \right] \right) + \hat{\xi} \frac{d\hat{j}}{d\hat{r}} + \hat{j} \frac{d\hat{\xi}}{d\hat{r}} + \frac{2}{\hat{r}} \hat{\xi} \hat{j}, \quad (15)$$

$$-\hat{v} \frac{d\hat{T}}{d\hat{r}} = \frac{Le}{Pe} \left(\frac{d^2 \hat{T}}{d\hat{r}^2} + \frac{2}{\hat{r}} \frac{d\hat{T}}{d\hat{r}} \right) + \frac{1}{St} \left(\frac{d\hat{j}}{d\hat{r}} + \frac{2}{\hat{r}} \hat{j} \right), \quad (16)$$

$$\frac{d\hat{T}}{d\hat{r}} = -Li_p \hat{g} \hat{\rho} \hat{T} - \frac{Li_\xi St}{R_\rho} \hat{T}^2 \frac{d\hat{\xi}}{d\hat{r}}. \quad (17)$$

where the dimensionless numbers are defined as

$$R_\rho = \frac{\rho^{sl}}{\rho_-^{sl}}, \quad R_v = \frac{\Delta V_{Fe}^{s,l}}{\Delta V_{Fe,O}^{s,l}}, \quad Li_p \equiv \frac{\Delta V_{Fe}^{s,l} g^{sl} \rho^{sl} r^{sl}}{L}, \quad Li_\xi \equiv \frac{1000 R \xi^{sl}}{a_O c_p},$$

$$Pe \equiv \frac{v_f r^{sl}}{D_O}, \quad St \equiv \frac{q^{sl}}{\rho_-^{sl} v_f L}, \quad Le \equiv \frac{k}{\rho^{sl} c_p D_O}. \quad (18)$$

R_ρ is the ratio between the reference density and the density on the solid side of the ICB, and R_v is the ratio between the change in specific volumes upon phase change of pure iron and the iron alloy. The dimensionless numbers Li_p and Li_ξ arise from the pressure and compositional parts of the liquidus constraint (17), respectively. Pe is the Péclet number that measures the ratio between advection and chemical diffusion. St is the Stefan number and gives the ratio between sensible and latent heat. Le is the Lewis number that describes the ratio between thermal and chemical diffusivity.

Inserting the scalings (14) into (8)–(13) yields the dimensionless boundary

conditions

$$\hat{T}(1) = \frac{T^{sl} c_p R_\rho}{StL}, \quad (19)$$

$$\left. \frac{d\hat{T}}{d\hat{r}} \right|_{\hat{r}=\frac{r^i}{r^{sl}}} = -\frac{Pe}{StLe}, \quad (20)$$

$$\left. \frac{d\hat{T}}{d\hat{r}} \right|_{\hat{r}=1} = -\frac{Pe}{Le}, \quad (21)$$

$$\hat{\xi}(1) = 1, \quad (22)$$

$$\hat{j}\left(\frac{r^i}{r^{sl}}\right) = -\hat{v}, \quad (23)$$

$$\hat{j}(1) = 0. \quad (24)$$

2.4. Model parameters and constraints

We solve the dimensionless system numerically using `solve_bvp`, which is a boundary value problem solver included in `scipy` – an open source Python library [28]. We rewrite the problem as a system of first-order ODEs, and vary the model parameters Pe , St , Le , Li_p , Li_ξ , R_ρ , R_v and T^{sl} (see Table 1). The numerical code written to solve the slurry equations is freely available online ¹. Unless otherwise specified, all other physical properties of the F-layer are assumed constant, as specified in Table A.2.

Pe varies because of the range of seismic estimates of the F-layer thickness, d , and the unknown freezing speed, v_f . We obtain a proxy for v_f through the ICB heat flow, Q^s , which we presume cannot be much greater than the adiabatic value estimated as $Q^a = 1.6$ TW [14], though we allow a wider margin of Q^s up to 3.2 TW to account for uncertainties also inherent in the estimate of Q^a in the literature. St varies due to Q^s and Q^{sl} . While there is no geophysical constraint on Q^{sl} , we test Q^{sl} over a wide range up to 12 TW which is verified *a posteriori*

¹<https://github.com/jnywong/nondim-slurry>

to give $5 \leq Q^c \leq 17$ TW [7, 29] (see Appendix C for the calculation of Q^c). Le depends on the thermal conductivity and we explore two values that represent the higher and the lower estimates given in the literature [13, 21, 30]. Li_p and R_ρ change according to the layer thickness and also the reference density, ρ^{sl} , though the density on the solid side of the ICB remains the same and is taken from PREM, $\rho_-^s = 12,764 \text{ kgm}^{-3}$. Li_ξ depends on ξ^{sl} , wherein the precise amount of oxygen present in the bulk of the Earth’s core is difficult to constrain with reported values varying between 0.1 and 11.0 mol.% for core chemistry models that include other light elements in addition to oxygen [31]. Varying ξ^{sl} between 2.0 and 12.0 mol.% changes R_v , which depends on both the layer thickness and the CSB oxygen concentration and in turn affects the change in specific volume between solid iron and the liquid iron alloy.

Input parameter	Symbol	Units	F-layer
Layer thickness	d	km	150, 200, 250, 300, 350, 400
Thermal conductivity	k	$\text{W m}^{-1}\text{K}^{-1}$	30, 100
ICB heat flux	Q^s	TW	0 – 3.20
CSB heat flux	Q^{sl}	TW	0 – 12
Sedimentation prefactor	k_ϕ	kgm^{-3}s	$10^{-5} - 10^{-1}$
CSB liquidus temperature	T^{sl}	K	4,500 – 6,000
CSB oxygen concentration	ξ^{sl}	mol.%	2 – 12
Péclet number	Pe		0 – 2500
Stefan number	St		0 – 3
Lewis number	Le		354 – 1196
Liquidus number (pressure)	Li_p		0.163 – 0.220
Liquidus number (compositional)	Li_ξ		0.004 – 0.028
Ratio between solid and reference density	R_ρ		0.940 – 0.952
Ratio between change in specific volumes upon phase change of pure iron and iron alloy	R_v		0.203 – 0.235

Table 1: Relevant dimensional and dimensionless parameter range for the F-layer, taking other physical parameters as constant given in Table A.2.

We constrain T^{sl} in boundary condition (19) from the melting curves of iron, which is usually reported in the range of 5,500 K [32] to 6,350 K [33]. Light

elements present in the iron alloy depress the liquidus temperature of pure iron, and a typical value of $\Delta T_\xi = 700$ K is used, though this can also vary between 500 and 1,000 K [31]. We therefore opt to vary T^{sl} between 4,500 and 6,000 K.

We constrain the results of the parameter study in three ways:

1. by the seismically determined density jump at the ICB [9]. The jump obtained from normal modes, $\Delta\rho_{\text{mod}}$, has a long wavelength on the order of hundreds of kilometres and represents the difference between the average densities of the top of the inner core and the bottom of the outer core. The jump obtained from body waves, $\Delta\rho_{\text{bod}}$, has a short wavelength on the order of several kilometres, and therefore represents the difference in densities either side of the ICB. The difference between the normal mode and body wave estimates therefore points to a density anomaly caused by the F-layer. Normal mode studies suggest $600 \text{ kg m}^{-3} \leq \Delta\rho_{\text{mod}} \leq 820 \pm 180 \text{ kg m}^{-3}$ [2, 34], whereas body wave studies suggest $520 \pm 240 \text{ kg m}^{-3} \leq \Delta\rho_{\text{bod}} \leq 1,100 \text{ kg m}^{-3}$ [35, 36]. Hence solutions obtained from the slurry model should satisfy a maximum density jump across the layer of $\max(\Delta\rho_{\text{mod}} - \Delta\rho_{\text{bod}}) = 1,000 - 280 = 720 \text{ kg m}^{-3}$, and a minimum bound $\min(\Delta\rho_{\text{mod}} - \Delta\rho_{\text{bod}}) < 0$ is not specified since the seismic observations from different studies vary in their approaches, so we consider zero as the lower bound.
2. solutions should be consistent with estimates of the present-day CMB heat flux, which should be between 5 and 17 TW [7, 29]
3. we assess the stability of the layer and determine whether the solution is stable, partially stable or unstable, and reject solutions that are unstable.

To apply the constraints on density we calculate the density jump across the slurry layer, $\rho_+^s - \rho^{sl}$, where ρ_+^s is the density on the slurry side of the ICB. The

total density is

$$\rho = \rho_H + \rho', \quad (25)$$

where

$$\rho_H = \left(\frac{g}{K}(r - r^{sl}) + \frac{1}{\rho^{sl}} \right)^{-1}, \quad (26)$$

is the hydrostatic part, in which K denotes the bulk modulus, and

$$\rho' = \rho^{sl} \left[-\alpha T' - \alpha_\xi \xi^{l'} + (\alpha_\phi + \alpha_\xi \xi^l) \phi' \right]. \quad (27)$$

is the density perturbation, where T' , $\xi^{l'}$ and ϕ' are perturbations in the decomposition

$$\begin{aligned} T &= T^{sl} + T', \\ \xi^l &= \xi^{sl} + \xi^{l'}, \\ \phi &= \phi^{sl} + \phi', \end{aligned}$$

with $\phi^{sl} = 0$ at the CSB. In the equation of state (27), the first two terms are well known from double diffusive/thermochemical convection theory, whereas the last term is unique to the slurry. The expansion coefficient of the solid is defined as

$$\alpha_\phi = \rho^{sl} \Delta V_{Fe,O}^{s,l},$$

(see derivation in Appendix D). To determine ϕ' , the dimensional solid flux yielded from the solution of the slurry equations is related to the solid fraction by

$$\mathbf{j} = b(\phi) \Delta V_{Fe,O}^{s,l} \nabla p. \quad (28)$$

We employ a Stokes' flow model of mobility [37] where we assume that the solid iron particles created in the slurry layer drift towards the ICB under the influence of gravity. Consequently the sedimentation coefficient is given by

$$b(\phi) = k_\phi \phi^{5/3} = \left(\frac{\rho_-^s (\rho^{sl})^2}{162\pi^2 \nu^3 N^2} \right)^{1/3} \phi^{5/3}, \quad (29)$$

where N is the number of particles in a unit volume. We write k_ϕ to group the prefactors that multiply the solid fraction. This k_ϕ sedimentation prefactor introduces a degree of freedom since N and the value of the kinematic viscosity, ν , in the slurry is unknown. We further consider this issue in Section 3.2, where we conduct a sensitivity analysis on k_ϕ .

We evaluate the gradient of the density perturbations to assess the stability of the layer. Solving the slurry equations yields T , ξ^l and ϕ and subtracting the reference values from these quantities gives the perturbations T' , ξ^l and ϕ' , which allows us to evaluate the density perturbation (27). If the layer is stable then the change in density relative to the hydrostatic reference should decrease as the radius increases, i.e. $d\rho'/dr < 0$, and vice versa if the layer is unstable, i.e. $d\rho'/dr > 0$. We relax the condition for stability slightly by stipulating that the layer is partially stable if $d\rho'/dr < 0$ for at least 100 km of the layer since the seismic resolution from normal modes is on the order of this value.

3. Results and discussion

3.1. Example solution

Figure 2 shows example solutions for a wide range of layer thicknesses between 150 and 400 km, where $Q^s = 2.5$ TW ($v_f = 0.44$ mmyr⁻¹), $Q^{sl} = 5$ TW, $k = 100$ Wm⁻¹K⁻¹ and $T^{sl} = 5,547$ K taken from [25, 27], for an 82%Fe-8%O-10%Si mixture. For all layer thicknesses the temperature gradient is strictly

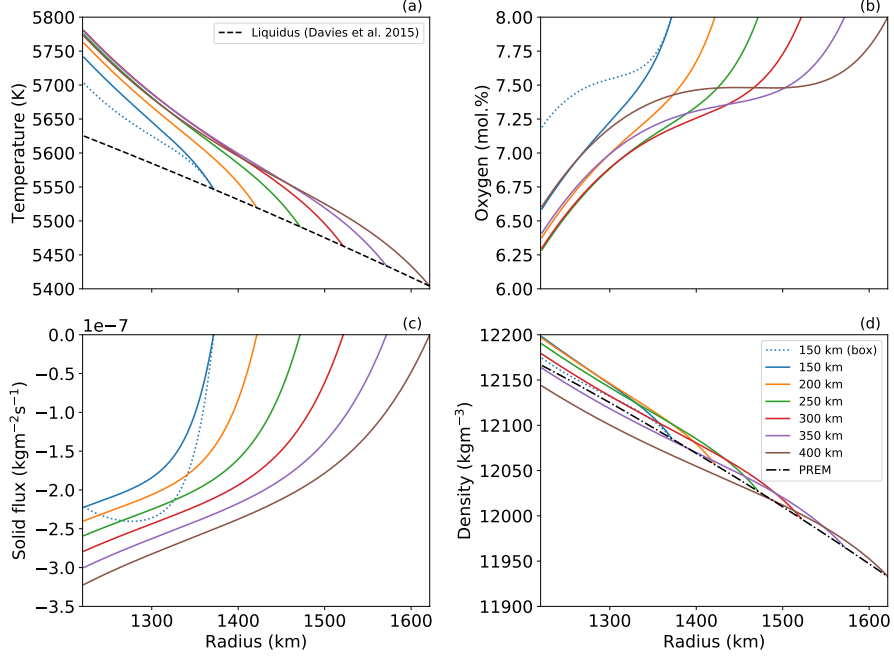


Figure 2: Profiles of (a) temperature, (b) oxygen concentration, (c) solid flux and (d) density across the slurry with layer thicknesses between 150 and 400 km. The dashed line in (a) is the uniform composition liquidus determined from *ab initio* calculations [25, 27], and the dash-dotted line in (d) is the PREM density [2]. The blue dotted line is the equivalent box model case from W18 for $d = 150$ km (see text). Control parameters are $Q^s = 2.5$ TW, $Q^{sl} = 5.0$ TW, $k = 100$ Wm $^{-1}$ K $^{-1}$ and $T^{sl} = 5,547$ K (colour online).

negative so the slurry is thermally destabilising, whereas the compositional gradient may either be stable or unstable. Solid flux is always negative in the direction towards the ICB, achieving its largest magnitude at the ICB itself and then vanishing to zero at the top of the layer as imposed by the boundary condition (24). Temperature, oxygen and solid flux all contribute to the overall density across the layer and the layer is stably-stratified when $150 \leq d \leq 300$ km, however for $d \geq 350$ km the layer is unstable.

We observe in Figure 2(c) that the solid flux eventually increases exponentially with radius under the influence of turbulent mixing from the bulk of the liquid outer core. As the solid flux diminishes its gradient sharply increases,

equivalent to precipitating more iron particles. The latent heat release associated with the phase change in the sublayer prompts the slurry to depress the temperature in Figure 2(a) to stay on the liquidus and the oxygen concentration gradient increases in response to this as seen in Figure 2(b).

For completeness, we compare the solution in spherical geometry for $d = 150$ km with the equivalent boundary conditions from the Cartesian geometry of W18, except for the box model we have shifted the CSB temperature to coincide with the liquidus value from [25, 27]. The main difference is that the effect of spherical geometry suppresses the effect of the mixing sublayer, since Figure 2(c) shows that the solid flux gradient in the upper part of the layer is shallower than the box model case. Melting at the base of the layer in the box model is highlighted by the negative gradient in the solid flux, which is not present in the spherical model, and contributes positively to the density variations at the base of the layer in the box model. Despite this, turbulent mixing in the sublayer dominates to depress the temperature and oxygen variations, producing a much smaller density difference overall in the box model.

The control parameters Pe and Li_p depend linearly on d and parameters R_ρ , R_v and Le depend indirectly on d through ρ^{sl} . For a sense of scale in the variation of parameters from $d = 150$ km to 400 km for the reference solution given in Figure 2, Pe increases by 18%, Li_p increases by 35%, R_v increases by 14% and the changes in R_ρ and Le are less than 1.5%. The combined effect of these changes strengthens the decay in temperature as a function of radius over the bulk of the layer (excluding the mixing sublayer), as seen in Figure 2(a), but decreases F and the strength of the turbulent mixing layer through the barodiffusion term in (15), as seen in Figure 2(c), which combine to reduce the magnitude of the density variations in the layer overall. Figure 3 shows more clearly that contributions to $d\rho'/dr$ from the oxygen gradient for

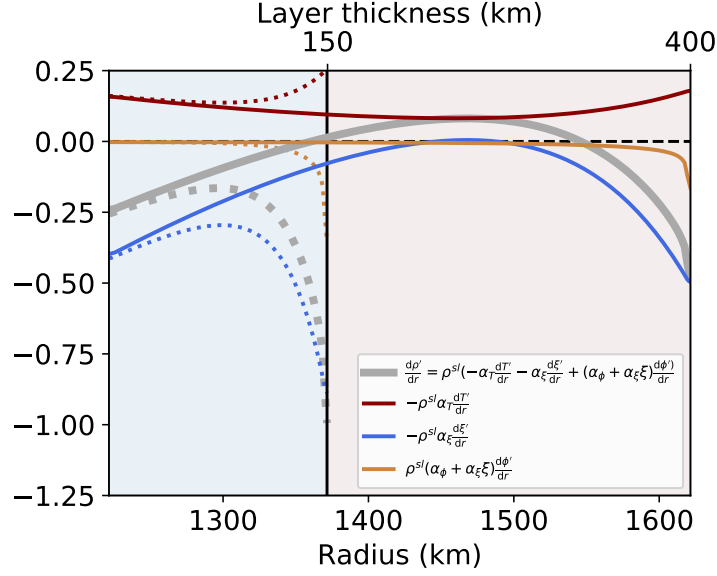


Figure 3: Gradients of the density variation (grey), $d\rho'/dr$, separated into contributions from the temperature (red), $-\rho^{sl}\alpha_T dT'/dr$, oxygen (blue), $-\rho^{sl}\alpha_\xi d\xi'/dr$, and solid fraction (orange), $\rho^{sl}(\alpha_\phi + \alpha_\xi \xi)d\phi'/dr$, across the slurry for layer thicknesses of 150 (dotted) and 400 km (solid). If $d\rho'/dr < 0$ the slurry is stable, whereas if $d\rho'/dr > 0$ the slurry is unstable. Control parameters are $Q^s = 2.5$ TW, $Q^{sl} = 5.0$ TW and $k = 100$ Wm $^{-1}$ K $^{-1}$ (colour online).

$d = 400$ km can become positive in the mid-depths, since the pressure part of the liquidus relation (17) outweighs the temperature part, before becoming negative again under the stabilising influence of the mixing sublayer. Oxygen variations predominantly control the gradient of the density variations. When $d = 400$ km the sign of $d\rho'/dr$ changes from negative (stable), to positive (unstable), and back to negative again, producing an “S”-shaped density profile seen in Figure 2(d). On the other hand, Figure 3 shows that for $d = 150$ km the layer is stable since $d\rho'/dr < 0$ throughout the layer. Overall variations in the solid fraction, ϕ' , are negligible over the majority of the layer, perhaps apart from a very thin region at the top (see Appendix B for further discussion on $d\phi$).

3.2. Sensitivity analysis

We evaluate the sensitivity of the slurry system to the sedimentation prefactor, k_ϕ , CSB temperature, T^{sl} , and CSB oxygen concentration, ξ^{sl} . We vary the value of k_ϕ by a large range between 10^{-5} and 10^{-1} kgm^{-3}s and recompute the example given in Figure 2(a) where the layer thickness is fixed at 150 km. Figure 4(a) shows that density stratification is increased with smaller values of k_ϕ and the solutions converge as k_ϕ exceeds 10^{-3} kgm^{-3}s . Figure 4(b) shows the corresponding solid fraction, ϕ , profiles within the layer. It can be seen that for the smallest value of k_ϕ , the solid fraction is close to the rheological transition at $\phi_m = 0.6$ [38], which violates the assumption that $\phi \ll 1$ in the slurry. We select a value of $k_\phi = 10^{-2}$ kgm^{-3}s that is high enough so that the density becomes independent of k_ϕ and consistent with $\phi \ll 1$ in the slurry.

For the CSB temperature, we recompute the example case with $d = 150$ km and vary T^{sl} between 4,500 and 6,000 K with intervals of 100 K and for the CSB oxygen concentration we vary its value between 2.0 and 12.0 mol.% with intervals of 0.5 mol.%. Figure 5(a) and (b) presents the density profiles across the layer with varying T^{sl} and ξ^{sl} , respectively. We find that no solutions were obtained for values below $\xi^{sl} = 2.0$ mol.%. Figure 5(b) shows that despite the variation in ξ^{sl} , there appears to be a limited effect on the resulting density profiles, whereas Figure 5(a) shows that changing T^{sl} introduces a greater spread in the solutions obtained. In terms of the dimensionless parameters, varying $2.0 \text{ mol.\%} < \xi^{sl} < 12.0 \text{ mol.\%}$ through $0.004 < Li_\xi < 0.028$ does not significantly affect the system, where Li_ξ enters into the pressure part of the liquidus relation and the barodiffusion term of equation (15). Changing T^{sl} in boundary condition (19) shifts the anchor point of the temperature solution and will not affect the curvature of the temperature profile since the heat fluxes into and out of the slurry remain fixed, so the temperature perturbations are the same for

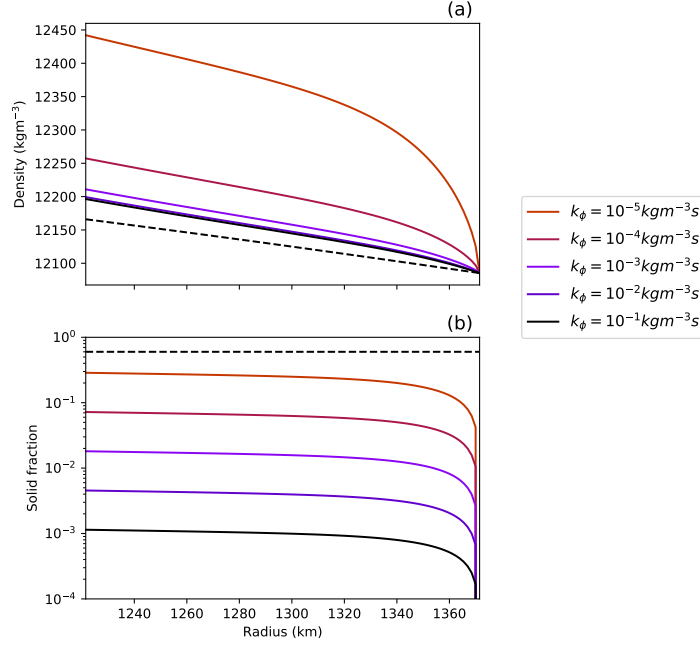


Figure 4: (a) Density and (b) solid fraction profiles across the layer for different values of k_ϕ . The dashed line in (a) is PREM and the dashed in (b) is $\phi_m = 0.6$ that defines the rheological transition [38]. All other input parameters are the same as the case in Figure 2 with the layer thickness fixed at 150 km (colour online).

all T^{sl} . However, T^{sl} does affect the oxygen concentration through the liquidus relation, where a higher T^{sl} will decrease the oxygen concentration gradient and create smaller perturbations in the oxygen concentration, therefore generating smaller density perturbations to produce a lower slurry density overall. A lower T^{sl} has the opposite effect to produce a higher slurry density. The spread in the ICB density with different T^{sl} is roughly 60 kgm⁻³, and there is up to a 40% change in the density jump across the whole layer with respect to the example case. This sensitivity may have an impact on the overall stability of the layer, however for the regime diagram we shall continue to use the default value from the literature of $T^{sl} = 5,547$ K for a layer 150 km thick.

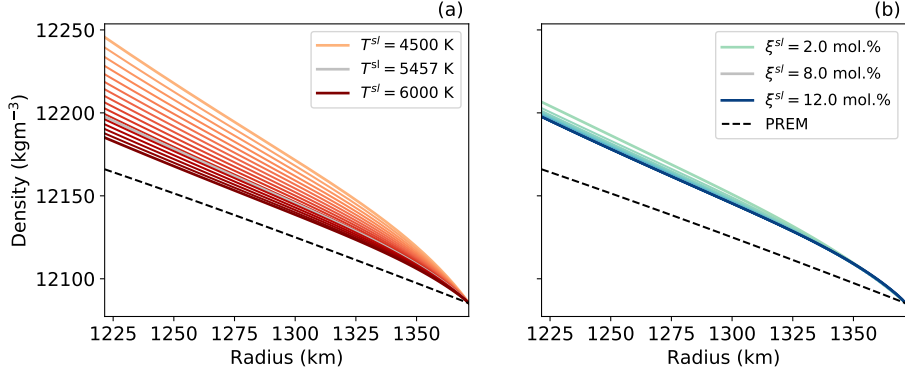


Figure 5: Density profiles across the layer for (a) $4,500 < T^{sl} < 6,000$ K and (b) $2.0 < \xi^{sl} < 12.0$ mol.%. Default values of $T^{sl} = 5,547$ K from [25, 27] in (a) and $\xi^{sl} = 8.0$ mol.% in (b) are given by the grey lines. All other input parameters are the same as the example case, and the layer thickness is fixed at 150 km (colour online).

3.3. Regime diagram

We present a regime diagram of the Pe, St -space by varying Q^s and Q^{sl} . There are two cases: high thermal conductivity, $k = 100 \text{ Wm}^{-1}\text{K}^{-1}$, corresponding to $Le = 1181$ and low thermal conductivity, $k = 30 \text{ Wm}^{-1}\text{K}^{-1}$, corresponding to $Le = 354$. By fixing $d = 150$ km and $\xi^{sl} = 8$ mol.%, then $Li_p = 0.16$, $Li_\xi = 0.018$, $R_\rho = 0.952$ and $R_v = 0.235$.

Figure 6(a) and (c) presents the regime diagram for the high Lewis number case, and Figure 6(b) and (d) is the regime diagram for the low Lewis number case. Regions of the phase space are divided into stable ($d\rho'/dr < 0$), partially stable ($d\rho'/dr < 0$ for at least 100 km) and unstable ($d\rho'/dr > 0$) slurries, and also areas with no slurry where no solution is found.

No slurry can exist when the latent heat release at the ICB interface exceeds the CSB heat flux, so that

$$\text{if } Q^{sl} < Q^s \quad \text{then} \quad St = \frac{q^{sl}}{q^s} < \left(\frac{r^i}{r^{sl}} \right)^2 \equiv St^*$$

which corresponds to a critical Stefan number of $0.6 \leq St^* \leq 0.8$ for 150 km \leq

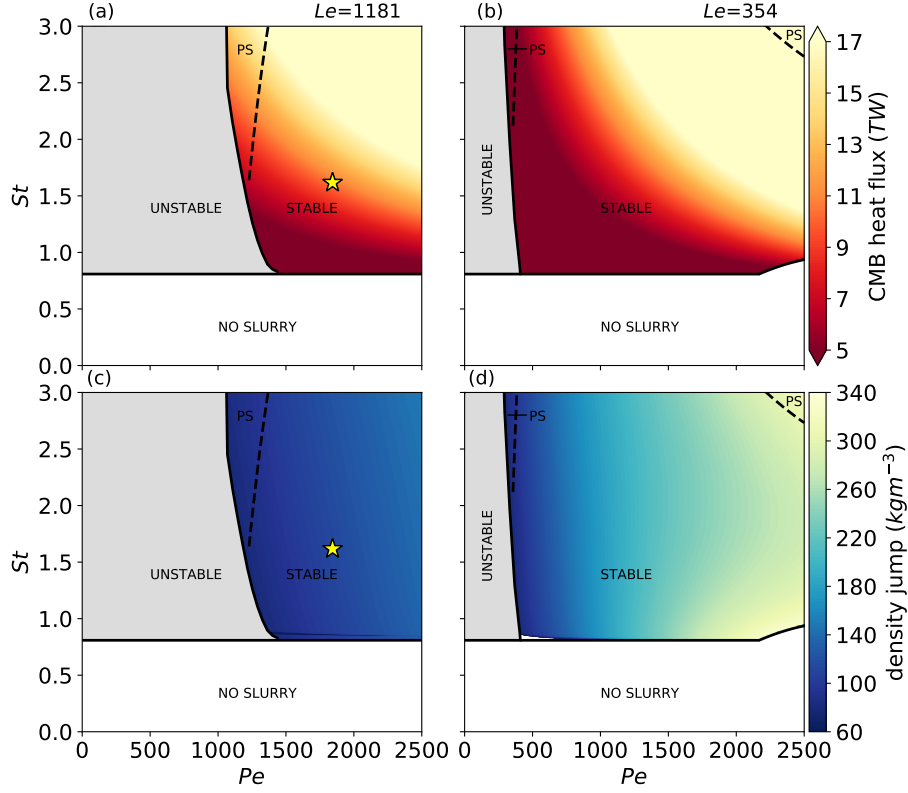


Figure 6: (Left column) Regime diagrams for the high Lewis number case, (right column) and the low Lewis number case with $d = 150$ km. (Top row) Contours of the CMB heat flux constrained by $5 < Q^c < 17$ TW and (bottom row) contours of the density jump, $\rho_+^s - \rho^{sl}$. The phase space is divided into stable (contour fill), partially stable, denoted PS (contour fill, dashed line), unstable (grey) and no slurry (white) regions. The yellow star represents the example case from Figure 2 (colour online).

$d \leq 400$ km. When the layer thickness is 150 km, above $St^* = 0.8$ we find a region of unstable solutions at lower Pe and stable solutions at higher Pe , and this transition generally occurs when

$$Pe_T \equiv \frac{Pe}{Le} = \frac{v_f r^{sl}}{\kappa} \simeq 1, \quad (30)$$

where Pe_T is the thermal Péclet number and $\kappa = k/\rho^{sl}c_p$ is the thermal diffusivity. Pe_T controls the boundary condition on the temperature gradient in

(20) and (21). An unstable slurry develops when $Pe < Le$ because more heat is conducted through the slurry which is unavailable for equilibration through the liquidus constraint, hence creating a smaller oxygen concentration difference that produces a smaller density contrast that is insufficient to stabilise the layer. A stable slurry develops when $Pe > Le$ as the rate of advection from the compacting layer overcomes the thermal diffusion rate. Increasing Pe_T stabilises the slurry layer since the temperature gradient steepens at the boundaries, therefore generating greater positive variations in the oxygen gradient that enhance the density anomaly. If $d = 150$ km then the transition at $Pe \simeq Le$ corresponds to $Q^s = 1.5$ TW for high Le and $Q^s = 0.5$ TW for low Le . Figure 6(c) and (d) show that the density jump across the layer in all cases is well below the maximum limit of 720 kgm^{-3} and also suggests that the density jump roughly scales with Pe , with higher values encountered at low Le .

A higher St steepens the CSB temperature gradient relative to the ICB, and condition (30) is met by strengthening the turbulent sublayer at the top of the slurry by increasing the mixing parameter F . Within the sublayer the rate of crystallisation is increased, therefore the density jump across the layer increases with St as seen in Figure 6(c) and (d). The critical Pe_T where the slurry transitions from unstable to stable slightly decreases as St increases and the layer is more likely to become partially stable. We find that the dimensionless ICB speed, and thereby the magnitude of the solid flux at the ICB, is roughly proportional to St . The ICB speed affects contributions to the secular cooling, gravitational power and latent heat release in the core and therefore influences the total CMB heat flow. This is reflected in Figure 6(a) and (b) on the total CMB heat flux, which scales linearly with $PeSt$.

3.4. Seismic properties of the F-layer and the inner core age

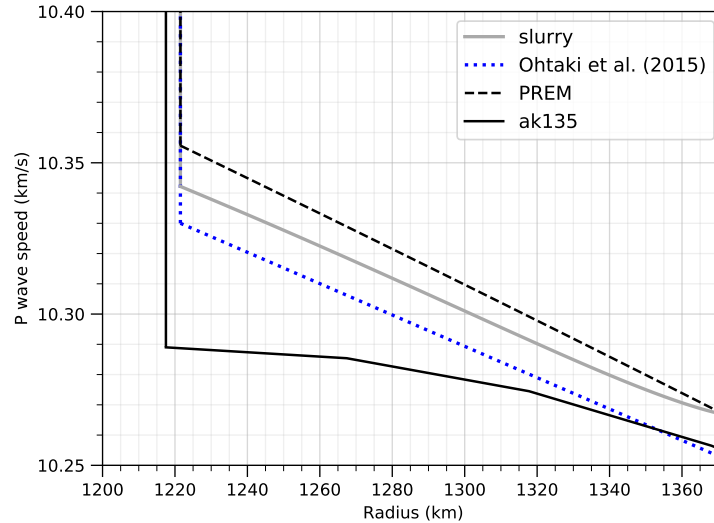


Figure 7: P wave speed in the F-layer derived from the high Le example solution with $d = 150$ km, $k = 100 \text{ Wm}^{-1}\text{K}^{-1}$, $Q^s = 2.5 \text{ TW}$ and $Q^{sl} = 5.0 \text{ TW}$ (grey, solid). Seismic models are PREM (black, dashed), ak135 (black, solid) and the FVW model of Ohtaki *et al.* [4] (blue, dotted) (colour online).

Motivated by the seismic observations, we have demonstrated that a slurry is able to produce stable layers with varying degrees of stratification depending on the parameters selected. If we invert the process, then what constraints can the model provide on observations? From our slurry model we can determine the density at every point across the layer and hence the P wave speed, $v_p^2 = K/\rho$. The bulk modulus, K , depends on the core chemistry and therefore an appropriate equation of state should be applied [19, 39]. For the sake of simplicity we approximate the bulk modulus by PREM in our calculations.

Figure 7 illustrates the v_p profile of the example solution from Section 3.1 compared with the seismic models of PREM [2], ak135 [40] and the FVW model of Ohtaki *et al.* [4]. The P wave speed from the slurry model is reduced relative to PREM by up to 0.13% and there is a difference of 0.1% compared with Ohtaki *et al.* [4], which reported that $v_p(r^i) = 10.3 \text{ km s}^{-1}$ and $dv_p/dr =$

$-5.2 \times 10^{-7} \text{ s}^{-1}$. For this example slurry solution we obtain a density jump across the layer of $\rho_+^s - \rho^{sl} = 112 \text{ kgm}^{-3}$ and calculate that $Q^c = 10.4 \text{ TW}$, which is within the acceptable range of CMB heat flows. On the slurry side of the ICB we have $\rho_+^s = 12,198 \text{ kgm}^{-3}$, therefore we predict that the density jump from body waves for this particular slurry is $\Delta\rho_{\text{bod}} = \rho_-^s - \rho_+^s = 502 \text{ kgm}^{-3}$. The density jump from normal modes is $\Delta\rho_{\text{mod}} = \Delta\rho_{\text{bod}} + \rho_+^s - \rho^{sl} = 628 \text{ kgm}^{-3}$, and this is fixed in all solutions of the slurry by choosing ρ_-^s and ρ^{sl} from PREM.

Note that the example solution given above is one of many compatible solutions given by the regime diagram. By considering the entire range of parameters permitted by the regime diagram that fit with the geophysical constraints, the high Le case gives $81 \leq \rho_+^s - \rho^{sl} \leq 140 \text{ kg m}^{-3}$ and the low Le case gives $101 \leq \rho_+^s - \rho^{sl} \leq 331 \text{ kg m}^{-3}$. This leads to bounds of $475 \leq \Delta\rho_{\text{bod}} \leq 534 \text{ kg m}^{-3}$ and $283 \leq \Delta\rho_{\text{bod}} \leq 513 \text{ kg m}^{-3}$ for high and low Le respectively. The observations available give $520 \pm 240 \leq \Delta\rho_{\text{bod}} \leq 1,100 \text{ kg m}^{-3}$, therefore our model suggests that a stably-stratified F-layer is opposed to the higher values of $\Delta\rho_{\text{bod}}$ recommended by the observations and that the slurry model gives an upper bound of $\Delta\rho_{\text{bod}} \leq 534 \text{ kg m}^{-3}$ for both Le cases.

We can approximate the inner core age using the model output of the ICB speed, v , by assuming that inner core growth is proportional to the square-root of time [41],

$$r^i(\tau) = r_0^i \left(1 + \frac{\tau}{\tau^i}\right)^{\frac{1}{2}}, \quad (31)$$

where τ is time normalised by the age of the inner core, τ^i , and r_0^i is the present-day IC radius. By differentiating (31) and considering the present-day where $\tau = 0$, we have

$$\tau^i = \frac{r_0^i}{2v}, \quad (32)$$

where we recall that $v \equiv v_f + v_s = dr^i/d\tau$ is the inner core growth rate. Estimating τ^i is of significant geophysical interest and its value is subject to debate since τ^i is directly related to the evolution of the core global heat balance, which is significantly affected by the thermal conductivity [21]. For the same range of solutions considered above to estimate $\Delta\rho_{\text{bod}}$, our results from the regime diagram for high Le give $0.52 \leq v \leq 0.98 \text{ mm yr}^{-1}$, which is relatively fast compared to the low Le solutions where $0.24 \leq v \leq 0.31 \text{ mm yr}^{-1}$. This yields an inner core age of $0.6 \leq \tau^i \leq 1.2 \text{ Ga}$ for high Le , which is in line with other estimates from the literature [7], and $2.0 \leq \tau^i \leq 2.6 \text{ Ga}$ for low Le , which is mostly beyond oldest estimates of 2.0 Ga from the literature using low thermal conductivity [27]. Our results therefore suggest a slurry model with high core conductivity predicts geophysical properties of the F-layer and core that are consistent with independent seismic and geodynamic calculations.

4. Conclusions

In this study, we have investigated the conditions that produce a stably-stratified slurry layer at the base of the Earth’s outer core. We non-dimensionalise the governing equations given by W18 and elucidate the key dimensionless parameters that control the system behaviour. By varying the Péclet and Stefan numbers, we map a regime diagram of the slurry demarcating the conditions that favour stable, partially stable and unstable density configurations, as well as no slurry. Solutions are obtained for high and low Le numbers, which reflect high or low thermal conductivity values of the core. We constrain the results by evaluating the density jump across the layer and the total CMB heat flux.

Our main result is that stably-stratified solutions can be produced by a slurry for a wide range of parameters that span plausible values for Earth’s core. We have identified regions of the parameter space containing many solutions that

are compatible with observations of the F-layer, and we have also established conditions that are not suitable. We find that

- $Pe_T = \frac{Pe}{Le} \simeq 1$ divides the space between unstable and stable slurry layers,
- higher Péclet number slurries generally facilitate stable density stratification because this controls the steepness of the temperature gradient at the boundaries, which in turn increases the magnitude of density variations in the slurry,
- the Stefan number has a stabilising role through crystallising more particles in the turbulent mixing sublayer,
- no slurry can exist with $St < St^* = (r^i/r^{sl})^2$ since the heat flow at the bottom of the layer is greater than at the top of the layer
- the slurry model suggests that $\Delta\rho_{\text{bod}} \leq 534 \text{ kg m}^{-3}$ for high and low Le
- estimates of the inner core age suggests a slurry with high core conductivity is compatible with independent estimates from the literature

Density perturbations of compositional origin dominate contributions to the overall stability of the layer, and can be destabilised through increasing the layer thickness. We have also investigated the sensitivity to the CSB temperature and oxygen concentration and deduced a limit for the prefactor $k_\phi = 10^{-2} \text{ kgm}^{-3}\text{s}$ that defines the sedimentation coefficient, $b(\phi)$, which relates the solid flux, \mathbf{j} , to the solid fraction, ϕ , through Stokes' flow. We find that the model is insensitive to the concentration of oxygen at the CSB, however, the effect of the liquidus temperature is significant to the overall stability of the layer.

From mineral physics or seismology of model uncertainties, improved estimates such as the layer thickness, CSB temperature and the CSB oxygen concentration, will benefit the slurry model greatly. Further progress determining

the liquidus curve for an iron mixture, using experiments or first-principle calculations, could improve the temperature condition at the CSB, and improved estimates of the density jump across the layer from normal and body wave studies would help constrain the space of geophysically consistent solutions.

We examined the P wave speed in the slurry layer to show that the model can produce a profile that compares well with other seismic models. This could be further verified comprehensively so that the model may provide a useful tool for corroborating observations, such as constraining the seismic density jump at the ICB derived from body waves, $\Delta\rho_{\text{bod}}$. There is also the potential for the slurry to provide improved and independent estimates of the inner core age stipulated by having a stable F-layer that agrees with the seismic and heat flow requirements.

We implemented a simple compacting layer on the solid side of the IC where solid particles produced by the slurry accumulate and instantly compact. Realistically the physics of this process is extremely complicated. Studies suggest that a mush solidification regime can occur [6] where liquid channels permeate a matrix of solid with a high solid fraction. A more advanced model may seek to incorporate this process. The timescale of interest in our slurry is comparable to the slow growth of the inner core, where we have applied the fast melting limit. On short timescales at the microscopic level, the effect of supercooling on the nucleation of solid iron at core conditions may come into play and this topic is an active area of interest [42, 43, 44].

Future work could focus on assessing the dominant balances between terms in the slurry equations that are responsible for stable density stratification so that the physics controlling the transitions between different regimes can be elucidated. For example, the importance of the mixing sublayer and its influence on the production of solid phase needs to be quantitatively evaluated. A more

sophisticated model coupling the slurry to outer core convection, perhaps similar to a recent study conducted by Bouffard *et al.* [45] for the stably-stratified layer at the top of the core, may fully capture the physics of this process and shed light on the effect of entrainment.

Our study also opted to keep the layer thickness constant over time in order to ascertain solutions that are concomitant with the present-day seismic observations. Relaxing the layer thickness requires an extra constraint on the model to be developed in its place [46]. Constructing a fully time-dependent framework could provide insight into the factors controlling the growth and decline of a slurry layer, which may shed light on how the F-layer came into existence over the core's history.

5. Acknowledgements

The numerical code used to solve the slurry equations in this paper is freely available at <https://github.com/jnywong/nondim-slurry>. We thank Marine Lasbleis and an anonymous reviewer for their constructive comments that helped improve this paper. JW acknowledges support from the Fondation Simone and Cino Del Duca of Institut de France and the Engineering and Physical Sciences Research Council (EPSRC) Centre for Doctoral Training in Fluid Dynamics (EP/L01615X/1). CJD is supported by the Natural Environment Research Council (NERC) Independent Research Fellowship (NE/L011328/1). Figures were produced using Matplotlib [47].

Appendix A. Table of values

Symbol	Definition	Value	Units	Source
p	Pressure		$\text{kgm}^{-1}\text{s}^{-2}$	
T	Temperature		K	
ξ	Light element concentration		Mass fraction	
ξ^l	Light element concentration in the liquid phase		Mass fraction	
ϕ	Solid fraction		Mass fraction	
j	Solid flux		$\text{kgm}^{-2}\text{s}^{-1}$	
ρ	Density		kgm^{-3}	
F	Mixing parameter			
v	ICB speed		ms^{-1}	
v_f	Freezing speed		ms^{-1}	
v_s	Snow speed		ms^{-1}	
μ	Chemical potential		Jkg^{-1}	
ρ_H	Hydrostatic density		kgm^{-3}	
ρ'	Density perturbation		kgm^{-3}	
T'	Temperature perturbation		K	
$\xi^{l'}$	Light element perturbation in the liquid phase		Mass fraction	
ϕ'	Solid fraction perturbation		Mass fraction	

$b(\phi)$	Sedimentation coefficient		kgm^{-3}s	
k_ϕ	Sedimentation coefficient prefactor		kgm^{-3}s	
ν	Kinematic viscosity		m^2s^{-1}	
N	No. of solid iron particles per unit volume			
Φ	Gibbs free energy			
Pe	Péclet number			
St	Stefan number			
Le	Lewis number			
Li_p	Liquidus number (pressure)			
Li_ξ	Liquidus number (composition)			
R_ρ	Ratio between liquid and solid iron			
R_v	Ratio between the change in specific volumes upon phase change from pure iron and iron alloy			
R	Ideal gas constant	8.31	$\text{Jkg}^{-1}\text{mol.}^{-1}$	
a_O	Atomic weight of oxygen	16	Da	
r^i	ICB radius	1221×10^3	m	PREM [2]

d	Layer thickness	(150, 200, 250, 300, 350, 400) $\times 10^3$	m	[3], [5]
r^{sl}	CSB radius	1371–1621 $\times 10^3$	m	[3], [5]
ρ_-^s	Density of iron on the solid side of the ICB	12.76×10^3	kgm^{-3}	PREM [2]
ρ_+^s	Density of iron on the liquid side of the ICB		kgm^{-3}	
ρ^{sl}	Density of liquid iron at $r = r^{sl}$		kg m^{-3}	PREM [2]
g	Gravity		ms^{-2}	PREM [2]
K	Bulk modulus		$\text{kgm}^{-1}\text{s}^{-2}$	PREM [2]
ξ^{sl}	Oxygen concentration in the bulk of the liquid core	2–12	mol.%	[31]
T^{sl}	Liquidus temperature at the CSB	4,500–6,000	K	[27, 25]
c_p	Specific heat capacity	715	$\text{Jkg}^{-1}\text{K}^{-1}$	[23]
α	Thermal expansion coefficient	1×10^{-5}	K^{-1}	[23]
α_ξ	Compositional expansion coefficient of oxygen	1.1		[24]
L	Latent heat of fusion	0.75×10^6	Jkg^{-1}	[23]
k	Thermal conductivity	30, 100	$\text{Wm}^{-1}\text{K}^{-1}$	[21], [27]

\bar{D}	Modified self-diffusion coefficient of oxygen		m^2s^{-1}	
D_O	Self-diffusion coefficient of oxygen	0.98×10^{-8}	m^2s^{-1}	[25]
V_{Fe}^s	Specific volume of solid iron		m^3kg^{-1}	Ideal solution theory
$V_{Fe,O}^l$	Specific volume of liquid iron and oxygen		m^3kg^{-1}	Ideal solution theory
$\Delta V_{Fe,O}^{s,l}$	Change in specific volume between liquid and solid phase		m^3kg^{-1}	Ideal solution theory
$\Delta V_{Fe}^{s,l}$	Change in specific volume between liquid iron and solid iron		m^3kg^{-1}	Ideal solution theory
α_ϕ	Expansion coefficient of solid			Ideal solution theory
q^s	ICB heat flow per unit area		Wm^{-2}	
q^{sl}	CSB heat flow per unit area		Wm^{-2}	
Q^s	ICB heat flow		TW	
Q^{sl}	CSB heat flow		TW	
Q^c	CMB heat flow	5–17	TW	[29], [7]
Q_s	Secular cooling		TW	
Q_g	Gravitational power		TW	
Q_l	Latent heat power		TW	

Table A.2: Symbols and values (if applicable) used in the slurry model. Group 1: fundamental thermodynamic variables. Group 2: slurry notation. Group 3: Dimensionless numbers. Group 4: Physical constants. Group 5: Seismic properties. Group 6: Properties determined from *ab initio* calculations and high-pressure experiments. Group 7: Properties that assume ideal solution theory. Group 8: Heat flow estimates.

Appendix B. Variations in the solid fraction, $d\phi$

We suppose that the variations in the solid fraction, $d\phi$, are negligible. Here we assess the validity of this assumption *a posteriori*. The variation in solid fraction enters the energy equation (2) and the equation of state (27). In the first instance, including these variations adds an extra term to the latent heat release due to phase change. The dimensionless energy equation (16) becomes

$$-\hat{v} \frac{d\hat{T}}{d\hat{r}} = \frac{Le}{Pe} \left(\frac{d^2\hat{T}}{d\hat{r}^2} + \frac{2}{\hat{r}} \frac{d\hat{T}}{d\hat{r}} \right) + \frac{1}{St} \left(\frac{d\hat{j}}{d\hat{r}} + \frac{2}{\hat{r}} \hat{j} - R_\rho \frac{d\phi}{d\hat{r}} \right).$$

Using the control parameters from Figure 3, we compare the order of magnitude of each part of the last term in the expression above where the $d\phi/d\hat{r}$ term appears. In Figure B.8 we can see that with $r^i/r^{sl} = 0.89$ and 0.75 (corresponding to $d = 150$ and 400 km, respectively), the extra term due to the variations in ϕ is almost three orders of magnitude smaller compared with the other two terms in the majority of the layer. We observe that $|\frac{2}{\hat{r}}\hat{j}| \sim |R_\rho \frac{d\phi}{d\hat{r}}|$ approaching the top of the layer, which is a consequence of \hat{j} tending to 0 as dictated by boundary condition $\hat{j}(1) = 0$ in equation (24). This occurs within a very thin region at the top of the layer and so $|R_\rho \frac{d\phi}{d\hat{r}}|$ makes a negligible difference to the overall energy balance in the slurry.

Turning to the equation of state we observe that the contributions from the variations in solid also arise by imposing boundary condition (24), which can

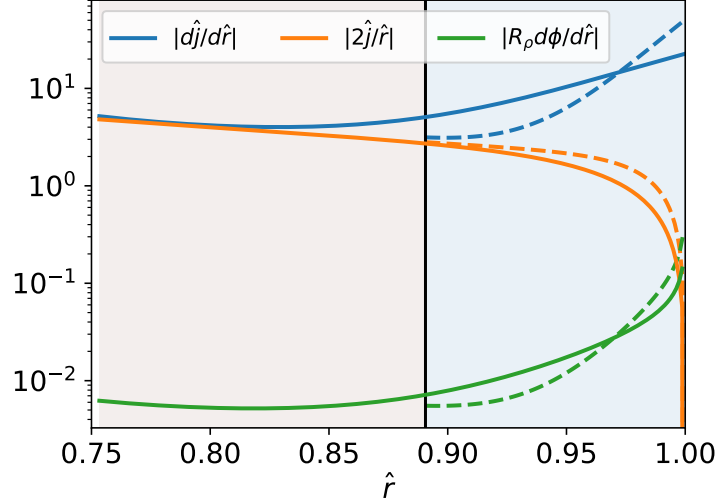


Figure B.8: Comparing magnitudes $|\frac{d\hat{j}}{d\hat{r}}|$, $|\frac{2}{\hat{r}}\hat{j}|$ and $|R_\rho \frac{d\phi}{d\hat{r}}|$, across the slurry for layer thicknesses of 150 (dashed, blue fill) and 400 km (solid). Control parameters are $Q^s = 2.5$ TW, $Q^{sl} = 5.0$ TW and $k = 100$ Wm⁻¹K⁻¹ (colour online).

be evaluated analytically by assuming Stokes' flow and writing

$$\lim_{\hat{r} \rightarrow 1} \left(\frac{d\phi}{d\hat{r}} \right) = \lim_{\hat{r} \rightarrow 1} \left(-\frac{3}{5} \left(\frac{\rho^s v_f}{K_\phi} \right)^{\frac{3}{5}} (-\hat{j})^{-\frac{2}{5}} \frac{d\hat{j}}{d\hat{r}} \right) = -\infty$$

On a physical basis Stokes' flow is unlikely to hold in the turbulent mixing region close to the CSB, and the contributions from the variations in ϕ in this thin region are considered to be a numerical artefact of maintaining $\hat{j}(1) = 0$. This thin region comprises less than 5% of the layer and has a limited impact on assessing the overall stability of the slurry.

Appendix C. CMB heat flow, Q^c

In general contributions to the CMB heat flux can be separated into the secular cooling, Q_s , gravitational power, Q_g , and the latent heat Q_l , while pressure freezing is neglected and radiogenic heating is ignored for the sake of

simplicity [24]. This gives a core heat balance of

$$Q^c = Q_s^l + Q_g^l + Q^{sl}, \quad (\text{C.1})$$

where

$$Q_s^l = -\frac{c_p}{T_c} \frac{dT_c}{dt} \int_{V^l} \rho T_a \, dV^l \quad (\text{C.2})$$

is the secular cooling in the liquid volume, V^l , and

$$Q_g^l = \int_{V^l} \rho \psi \alpha_\xi \frac{d\xi}{dt} \, dV^l - 4\pi (r^{sl})^2 \rho^{sl} \psi^{sl} \alpha_\xi \xi^{sl} v \quad (\text{C.3})$$

is the gravitational power in the liquid volume, and Q^{sl} is the heat flux imposed at the CSB that also contains Q_l . In (C.2), the adiabatic temperature is given by [23]

$$T_a(r) = T^{sl} \exp\left(-\int_{r^{sl}}^r \frac{g\gamma}{\phi} \, dr\right). \quad (\text{C.4})$$

We calculate the core cooling rate, dT_c/dt , by constructing an adiabat anchored at the present day CSB temperature, followed by constructing a new adiabat anchored at a new CSB temperature after time Δt due to the advancing layer, and then finding the resulting decrease in the CMB temperature, $T_c = T_a(r_c)$.

This is given by

$$\frac{dT_c}{dt} \approx \frac{\Delta T_c}{\Delta t} = \frac{T^{sl}(r^{sl} + v\Delta t) \exp\left(-\int_{r^{sl}+v\Delta t}^{r_c} \frac{g\gamma}{\phi} \, dr\right) - T^{sl}(r^{sl}) \exp\left(-\int_{r^{sl}}^{r_c} \frac{g\gamma}{\phi} \, dr\right)}{\Delta t}.$$

The gravitational power (C.3), is composed of two parts: the first part is proportional to the change in oxygen concentration in the bulk of the volume, V^l , and the second part is from the motion of the CSB, where there is no additional

contribution from the motion of the ICB since the CSB and ICB move at the same rate. By mass conservation, the change in oxygen concentration in the bulk is given by

$$\int_{V^l} \frac{\partial \xi}{\partial t} dV^l = \frac{-4\pi(r^{sl})^2 \rho^{sl} \xi^{sl} v}{M_l},$$

where $M_l = \int_{V^l} \rho dV^l$ is the mass of the liquid outer core.

Appendix D. Definition of the solid expansion coefficient, α_ϕ

The coefficient, α_ϕ , is a dimensionless expansion coefficient that influences the contribution of the solid fraction to the slurry density. From equation (A3) of W18, we have that

$$\alpha_\phi \equiv -\rho^{sl} \left(\frac{\partial V}{\partial \phi} \right)_{p,T,\xi}. \quad (\text{D.1})$$

From (A1) of W18, the expression for the Gibbs free energy, $d\Phi$, defines the specific volume as

$$V \equiv \left(\frac{\partial \Phi}{\partial p} \right)_{T,\xi,\phi}. \quad (\text{D.2})$$

The lever rule in equation (A9) of W18 gives

$$\left(\frac{\partial \Phi}{\partial \phi} \right)_{p,T,\xi} = \Phi^s - \Phi^l \quad (\text{D.3})$$

and

$$\left(\frac{\partial \Phi^s}{\partial p} \right)_{T,\xi,\phi} = V_{Fe}^s, \quad \left(\frac{\partial \Phi^l}{\partial p} \right)_{T,\xi,\phi} = V_{Fe,O}^l, \quad (\text{D.4})$$

where Φ^s is the solid part of the Gibbs free energy and Φ^l is the liquid part. Substituting (D.2), (D.3) and (D.4) into (D.1) gives the final result

$$\alpha_\phi = -\rho^{sl} (V_{Fe}^s - V_{Fe,O}^l) = \rho^{sl} \Delta V_{Fe,O}^{s,l}. \quad (\text{D.5})$$

References

- [1] C. M. Hardy, J. Wong, Stably stratified layers within Earth’s core, *Astronomy & Geophysics* 60 (3) (2019) 3–30.
- [2] A. Dziewonski, D. Anderson, Preliminary Reference Earth Model, *Phys. Earth Planet. Int.* 25 (1981) 297–356.
- [3] A. Souriau, G. Poupinet, The velocity profile at the base of the liquid core from PKP(BC+Cdiff) data: an argument in favor of radial inhomogeneity, *Geophys. Res. Lett.* 18 (1991) 2023–2026.
- [4] T. Ohtaki, S. Kaneshima, Independent estimate of velocity structure of Earth’s lowermost outer core beneath the northeast Pacific from PKiKP–PKPbc differential traveltimes and dispersion in PKPbc, *Journal of Geophysical Research: Solid Earth* 120 (11) (2015) 7572–7586.
- [5] Z. Zou, K. Koper, V. Cormier, The structure of the base of the outer core inferred from seismic waves diffracted around the inner core, *J. Geophys. Res.* 113 (2008) B05314.
- [6] R. Deguen, Structure and dynamics of Earth’s inner core, *Earth Planet. Sci. Lett.* 333–334 (2012) 211–225.
- [7] F. Nimmo, Energetics of the core, in: G. Schubert (Ed.), *Treatise on Geophysics* 2nd Edn, Vol. 9, Elsevier, Amsterdam, 2015, pp. 31–65.

- [8] T. Alboussière, R. Deguen, Asymmetric dynamics of the inner core and impact on the outer core, *J. Geodyn.* 61 (2012) 172–182.
- [9] D. Gubbins, G. Masters, F. Nimmo, A thermochemical boundary layer at the base of Earth’s outer core and independent estimate of core heat flux, *Geophys. J. Int.* 174 (2008) 1007–1018.
- [10] D. Loper, P. Roberts, On the motion of an iron-alloy core containing a slurry: I. General theory, *Geophys. Astrophys. Fluid Dyn.* 9 (1977) 289–321.
- [11] J. Wong, C. J. Davies, C. A. Jones, A Boussinesq slurry model of the F-layer at the base of Earth’s outer core, *Geophysical Journal International*.
- [12] N. de Koker, G. Steinle-Neumann, V. Vojtech, Electrical resistivity and thermal conductivity of liquid Fe alloys at high P and T and heat flux in Earth’s core, *Proc. Natl. Acad. Sci.* 109 (2012) 4070–4073.
- [13] M. Pozzo, C. Davies, D. Gubbins, D. Alfè, Thermal and electrical conductivity of iron at Earth’s core conditions, *Nature* 485 (2012) 355–358.
- [14] M. Pozzo, C. Davies, D. Gubbins, D. Alfè, Thermal and electrical conductivity of solid iron and iron-silicon mixtures at Earth’s core conditions, *Earth Planet. Sci. Lett.* 393 (2014) 159–164.
- [15] R. Deguen, T. Alboussière, S. Labrosse, Double-diffusive translation of Earth’s inner core, *Geophysical Journal International* 214 (1) (2018) 88–107.
- [16] D. Loper, P. Roberts, A Boussinesq model of a slurry, *Structure and Dynamics of Partially Solidified Systems* (1987) 291–323.
- [17] F. Birch, Elasticity and the constitution of Earth’s interior, *J. Geophys. Res.* 66 (1952) 227–286.

- [18] D. Alfè, M. Gillan, G. Price, Composition and temperature of the Earth's core constrained by combining *ab initio* calculations and seismic data, *Earth Planet. Sci. Lett.* 195 (2002) 91–98.
- [19] J. Badro, A. Côté, J. Brodholt, A seismologically consistent compositional model of Earth's core, *Proc. Natl. Acad. Sci.* 111 (2014) 7542–7545.
- [20] H. Gomi, K. Ohta, K. Hirose, S. Labrosse, R. Caracas, V. Verstraete, J. Hernlund, The high conductivity of iron and thermal evolution of the Earth's core, *Phys. Earth Planet. Int.* 224 (2013) 88–103.
- [21] Q. Williams, The thermal conductivity of Earth's core: A key geophysical parameter's constraints and uncertainties, *Annual Review of Earth and Planetary Sciences* 46 (1).
- [22] R. Deguen, T. Alboussière, D. Brito, On the existence and structure of a mush at the inner core boundary of the Earth, *Phys. Earth Planet. Int.* 164 (2007) 36–49.
- [23] D. Gubbins, D. Alfe, G. Masters, G. Price, M. Gillan, Can the Earth's dynamo run on heat alone?, *Geophys. J. Int.* 155 (2003) 609–622.
- [24] D. Gubbins, D. Alfè, G. Masters, G. Price, M. Gillan, Gross thermodynamics of two-component core convection, *Geophys. J. Int.* 157 (2004) 1407–1414.
- [25] M. Pozzo, C. Davies, D. Gubbins, D. Alfè, Transport properties for liquid silicon-oxygen-iron mixtures at Earth's core conditions, *Phys. Rev. B* 87 (2013) 014110.
- [26] C. Davies, Cooling history of Earth's core with high thermal conductivity, *Phys. Earth Planet. Int.*

- [27] C. Davies, M. Pozzo, D. Gubbins, D. Alfè, Constraints from material properties on the dynamics and evolution of Earth’s core, *Nat. Geosci.* 8 (2015) 678–687.
- [28] P. Virtanen, R. Gommers, T. Oliphant, M. Haberland, T. Reddy, D. Cournapeau, E. Burovski, P. Peterson, W. Weckesser, J. Bright, et al., Scipy 1.0: fundamental algorithms for scientific computing in Python, *Nature methods* 17 (3) (2020) 261–272.
- [29] T. Lay, J. Hernlund, B. Buffett, Core-mantle boundary heat flow, *Nat. Geosci.* 1 (2008) 25–32.
- [30] F. Stacey, D. Loper, A revised estimate of the conductivity of iron alloy at high pressure and implications for the core energy balance, *Phys. Earth Planet. Int.* 161 (2007) 13–18.
- [31] K. Hirose, S. Labrosse, J. Hernlund, Compositional state of Earth’s core, *Annual Review of Earth and Planetary Sciences* 41 (2013) 657–691.
- [32] R. Sinmyo, K. Hirose, Y. Ohishi, Melting curve of iron to 290 GPa determined in a resistance-heated diamond-anvil cell, *Earth and Planetary Science Letters* 510 (2019) 45–52.
- [33] J. Jackson, W. Sturhahn, M. Lerche, J. Zhao, T. Toellner, E. Ercan Alp, S. Sinogeikin, J. Bass, C. Murphy, J. Wicks, Melting of compressed iron by monitoring atomic dynamics, *Earth Planet. Sci. Lett.* 362 (2013) 143–150.
- [34] G. Masters, D. Gubbins, On the resolution of density within the Earth, *Phys. Earth Planet. Int.* 140 (2003) 159–167.
- [35] K. D. Koper, M. Dombrovskaya, Seismic properties of the inner core boundary from PKiKP/P amplitude ratios, *Earth Planet. Sci. Lett.* 237 (2005) 680–694.

- [36] H. Tkalčić, B. Kennett, V. Cormier, On the inner–outer core density contrast from PKiKP/PcP amplitude ratios and uncertainties caused by seismic noise, *Geophys. J. Int.* 179 (2009) 425–443.
- [37] D. Loper, P. Roberts, On the motion of an iron-alloy core containing a slurry: II. A simple model, *Geophys. Astrophys. Fluid Dyn.* 16 (1980) 83–127.
- [38] V. Solomatov, Magma oceans and primordial mantle differentiation., in: G. Schubert, B. Romanowicz, A. Dziewonski (Eds.), *Treatise on geophysics*, Elsevier, Amsterdam, 2015, pp. 655–693.
- [39] S. Cottaar, T. Heister, I. Rose, C. Unterborn, Burnman: A lower mantle mineral physics toolkit, *Geochemistry, Geophysics, Geosystems* 15 (4) (2014) 1164–1179.
- [40] B. Kennett, E. Engdahl, R. Buland, Constraints on seismic velocities in the Earth from traveltimes, *Geophys. J. Int.* 122 (1995) 108–124.
- [41] S. Labrosse, Thermal and compositional stratification of the inner core, *C. R. Geosci.* 346 (2014) 119–129.
- [42] L. Huguet, J. Van Orman, S. Hauck II, M. Willard, Earth’s inner core nucleation paradox, *Earth Planet. Sci. Lett.* 487 (2018) 9–20.
- [43] C. J. Davies, M. Pozzo, D. Alfè, Assessing the inner core nucleation paradox with atomic-scale simulations, *Earth and Planetary Science Letters* 507 (2019) 1–9.
- [44] M. Lasbleis, M. Kervazo, G. Choblet, The fate of liquids trapped during the Earth’s inner core growth, *arXiv preprint arXiv:1912.12258*.
- [45] M. Bouffard, M. Landeau, A. Goument, Convective erosion of a primordial stratification atop Earth’s core, *Geophysical Research Letters*.

- [46] J. Wong, A slurry model of the f-layer in the earth's core, Ph.D. thesis, University of Leeds (2018).
- [47] J. D. Hunter, Matplotlib: A 2D graphics environment, *Computing in Science & Engineering* 9 (3) (2007) 90–95. doi:10.1109/MCSE.2007.55.